nature portfolio

https://doi.org/10.1038/s41561-020-00684-y

Supplementary information

Implications of the iron oxide phase transition on the interiors of rocky exoplanets

In the format provided by the authors and unedited

Supplementary Information

Implications of the iron oxide phase transition on the interiors of rocky exoplanets

F. Coppari[1*], R. F. Smith[1], J. Wang[2], M. Millot[1], D. Kim[2], J. R. Rygg[3,4,5], S. Hamel[1], J. H. Eggert[1], T. S. Duffy[2]

[1] *Lawrence Livermore National Laboratory, Livermore, CA, USA*

[2] *Princeton University, Department of Geosciences, Princeton, NJ, USA*

[3] *Laboratory for Laser Energetics, Rochester, NY, USA*

[4] *Department of Mechanical Engineering, University of Rochester, Rochester, NY, USA*

[5] *Department of Physics and Astronomy, University of Rochester, Rochester, NY, USA*

[*] coppari1@llnl.gov

CONTENTS

I. FeO TEMPERATURE IN DYNAMIC RAMP COMPRESSION

Quasi-isentropic ramp-compression is a well controlled technique to compress materials to ultrahigh pressures in the solid phase. Compared to single shock compression (which generates states along the Hugoniot curve), ramp compression drastically reduces the temperature increase induced by the ultrafast wave propagation. This is obtained by decomposing the compression into multiple steps, and in the experiments discussed here, achieved by combining a gradually increasing laser power profile with a specific target configuration, where the sample material is enclosed between two stiff diamond plates. As demonstrated in a number of studies on different materials, where X-ray diffraction signatures for solids have been measured at pressures well above the Hugoniot melting[14,55,56,61–64] (i.e. the pressure at which melting occurs upon a single shock propagation), this compression technique allows us to reach extreme pressure states while keeping the material in the solid state. While a perfect shockless compression would follow the material isentrope, the ramp-compression realized in the experiments reported here, achieve higher temperatures due to the combination of formation of small shocks and strength effects[65].

A direct temperature measurement is currently not possible with our diffraction experimental platform. We can, however, place bounds on possible temperature.

Comparing the density of B2-FeO obtained in our lowest-pressure experiment at 357 GPa with the results of high-temperature diamond anvil cell (DAC) diffraction experiments from Ozawa *et al*[13] around 300 GPa and 3000-4000 K (Figs. 3 and 6) we observe that our data under ramp compression are characterized by similar density as Ozawa's data within uncertainty. This suggests that the temperature in our measurements should not be significantly higher than ∼4000 K, which is the maximum temperature obtained in the laser-heated DAC experiments.

This estimate is also in agreement with the extrapolation of the FeO melting curve (black dashed line in Supplementary Fig. 6 from[66]) in the pressure range 300-700 GPa, that provides us with an upper bound to the temperature of our measurements to be ∼6000 K.

The lower temperature bound can be constrained considering the FeO phase diagram as measured in high pressure and high temperature diamond anvil cells experiments (Supplementary Fig. 6). According to the location of the B8-B2 phase boundary from literature data[13] and our observation of the B2 structure at 357 GPa (experiment 68984) we can conclude that our data should be above ∼2000 K.

Based on these arguments we represent the expected temperature conditions of our ramp diffraction data with the shaded dark-blue circle in Supplementary Fig. 6.

It is important to point out that single shock compression of FeO would result in the melting of the sample at about 200 GPa (arrow in Supplementary Fig. 6), as inferred by the extrapolation of shock data[67], represented by black circles in Supplementary Fig. 6.

II. IDENTIFICATION OF DIFFRACTION SIGNAL FROM DIAMOND

In Supplementary Fig. 4 we report X-ray diffraction data from one of our experiments (68948). The data have been background-subtracted and show portions of the diffraction arcs as collected in two image plate detectors surrounding the sample[55,56]. The data illustrate the specific character of the signal associated with the different diffracting components present in the target assembly. The polycrystalline FeO sample is sandwiched between single-crystal diamonds used as ablator and window. The quasi-monochromatic X-ray source can generate Bragg diffraction of compressed single-crystal diamond, that under ramp-compression fragments, forming multiple crystallites. The resulting signal (highlighted by the red circle) is highly textured and localized, as opposed to the extended lines of the polycrystalline Ta and FeO. Note that because the diamonds are not at uniform pressure state when the X-ray source is generated (Supplementary Fig. 5c), their diffraction signal is quite broad and may also consist of distinct peaks (experiments 72648 and 73143 in Supplementary Fig. 2.) We also observe Laue diffraction from diamond (blue circle in image on the left). This is because the X-ray sources generated by laser-irradiated foils produce a continuous broadband X-ray background, in addition to the quasi-monochromatic He-α line emission, that may be bright enough to create a detectable Laue diffraction signal off of single-crystal diamonds[53]. The Laue spots may be very intense and may overlap with the main diffraction peaks, therefore they are normally masked out before integrating the diffraction data. Because of the striking difference between the diffraction signal originating from the diamond (either Bragg or Laue diffraction) and from the randomly-oriented FeO powder (Supplementary Fig. 4), there is no ambiguity in the peak assignment.

III. DETERMINATION OF THE HIGH-PRESSURE STRUCTURE OF FeO

New FeO stoichiometries have been predicted to arise at high pressure and have also been documented in diamond anvil cell experiments at high pressure and temperature.

Lavina *et al*[32] reported high pressure/temperature synthesis of a recoverable Fe_4O_5 form. The diffraction data show that this compound has an orthorhombic unit cell with space group *Cmcm*. Being a low-symmetry structure its diffraction pattern is characterized by many peaks of comparable intensities (Supplementary Material of Ref.[32]) that is not consistent with our data showing only two distinct reflections.

Hu *et al*[33] identified a new pyrite-structure (FeO_2) at 76 GPa and 1800 K, also supported by first principle calculations.

Calculations using Density Functional Theory (DFT) and random structural searching have examined addi-

tional possible high pressure structures for iron oxide and found the stabilization of new stoichiometries[31]. According to this work, in the pressure range explored in our study, the most stable candidates are Fe_2O (space group $I4/mmm$), stochiometric FeO (space group $R\bar{3}m$) and Fe_2O_3 (space group $P2_12_12_1$) at 350 GPa and FeO_2 (space group $R\bar{3}m$) and FeO_4 (space group $P2_1/c$) at 500 GPa. Weerasinghe *et al*[31] also predicted the formation of FeO_2 with space group $Pa\bar{3}$ below 100 GPa which corresponds to the structure found experimentally at 76 GPa and 1800 K by Hu *et al*[33]. According to the DFT study this structure is stable up to 465 GPa and transforms to FeO_2 with space group $R\bar{3}m$ at higher pressure.

We compared our experimental results with these predictions and we found that our data are best interpreted by the formation of B2-FeO in the 300-700 GPa pressure range. It is important to point out that such calculations were performed at 0 K and finite temperature effects on phase stability could be at the origin of the discrepancy with the observation of B2-FeO in high pressure and temperature experiments.

Comparison of the expected diffraction signals for the structures predicted in Ref.[31] with our data as well as their *d*-spacings with the measured ones show that our data are best interpreted as a transformation to the B2 phase (Supplementary Fig. 7) rather than the newly proposed ones.

In each of Supplementary Figs. 7 - 13 the top panel shows the comparison of the simulated diffraction signal (intensity vs diffraction angle 2θ) for the theoretically predicted structure (grey) and the experimental one at a similar pressure (blue). The simulated diffraction signals have been calculated using the experimental X-ray wavelength (see figure legend) and a 0.8° broadening, representative of the experimental angular resolution[53,55,56]. The bottom panel shows the comparison in *d*-spacing vs pressure: grey triangles represent the reflections corresponding to the simulated structure, while blue circles correspond to our experimental measurements. Other symbols are: red markers for the B1 phase (triangles from[24], squares from[29] and dashed line from[30]); yellow symbols for the B8 structure (crosses from[26], triangles from[27] and yellow bands correspond to varying 2<c/a<2.06 from[30]); cyan and blue squares for room and high temperature B2 phase from[13]. The dashed blue line is calculated from the fit to the B2 data from this work and high temperature DAC experiments.

IV. DENSITY AND PSEUDO-EOS OF B2-FeO

We use a Vinet equation of state (EOS) to fit the pressure-density data for B2-FeO, fitting together our dataset and the one from Ref.[13] to obtain the bulk modulus (K_0), its pressure derivative (K_0'), as well as the density of the high pressure B2-FeO phase extrapolated at ambient pressure (ρ_0). The fitting results are reported in Supplementary Table 2 and compared with values for the B1 and B8 structures as reported in literature[30]. It is interesting to note that the extrapolated density of B2-FeO is not significantly different than the initial density of wüstite, in contrast to B2-MgO that shows about 4% higher density than periclase[14]. This is reflected in the absence of a large volume discontinuity across the B1/B8/B2 phase transitions. It is also important to point out that in our ramp-compression data each experiment is characterized by a slightly different temperature, therefore fitting the measured pressure-density relation to an equation of state is only intended in a qualitative sense or as a pseudo-equation-of-state.

The density values reported in Fig. 3 and Supplementary Table 3 are obtained from the measured *d*-spacings assuming a molecular weight for FeO of 71.844 g/mol, corresponding to stoichiometric composition. Although the initial composition of our sample is $Fe_{0.94}O$, pressure and temperature are known to induce compositional changes, favoring the increase of the iron concentration[23,68,69], owing to the pressure-induced volume reduction which makes vacancies energetically unfavorable. The uncertainty in the final composition of our sample is reflected in a density uncertainty represented by the hatched shaded area in Fig. 3, which has been calculated assuming a molar weight ranging from 68.494 g/mol to 71.844 g/mol and corresponding to the initial $Fe_{0.94}O$ stoichiometry and stoichiometric FeO, respectively.

V. IDEAL BINARY SOLUTION MODEL FOR THE MgO-FeO SYSTEM

We utilize the formalism described in previous reports[70,71] and consider ideal mixing of MgO and FeO that has been proven appropriate to describe the B1-B2 transition in salts[70] and has been widely used in geological systems including ferropericlase[36,39,71].

For each end-member of the $(Mg_x,Fe_{(1-x)})O$ solid solution, equilibrium between the B1 and B2 structures requires the chemical potential of the two phases to be equal:

$$\mu^{B1}_{MgO}(P) - \mu^{B2}_{MgO}(P) = 0 \quad (1)$$

$$\mu^{B1}_{FeO}(P) - \mu^{B2}_{FeO}(P) = 0 \quad (2)$$

Assuming ideal mixing of MgO and FeO and no pressure dependence of the volume change across the phase transition, because $\Delta H_{mix} = 0$, eq. 1 and 2 can be rewritten as:

$$2RT \ln \frac{\alpha^{B1}_{MgO}}{\alpha^{B2}_{MgO}} + \Delta V_{MgO}(P - P^t_{MgO}) = 0$$

$$2RT \ln \frac{\alpha^{B1}_{FeO}}{\alpha^{B2}_{FeO}} + \Delta V_{FeO}(P - P^t_{FeO}) = 0$$

where $\Delta V_{MgO} = V^{B1}_{MgO} - V^{B2}_{MgO}$ and $\Delta V_{FeO} = V^{B1}_{FeO} - V^{B2}_{FeO}$ are the volume differences at the B1/B2 phase transition in MgO and FeO, P^t_{MgO} and P^t_{FeO} their transition

pressures and the factor 2 originates from the two different atomic species of the end-members. α represents the activity of the end-members for the two phases. For an ideal binary solution the activity of a component with a given phase equals its mole fraction ($\alpha^{B1}_{MgO} = x^{B1}_{MgO}$, and similarly for FeO and for the B2 phase), therefore:

$$\ln \frac{x^{B1}}{x^{B2}} = \frac{1}{2RT}\Delta V_{MgO}(P^t_{MgO} - P) \quad (3)$$

and

$$\ln \frac{(1-x^{B1})}{(1-x^{B2})} = \frac{1}{2RT}\Delta V_{FeO}(P^t_{FeO} - P) \quad (4)$$

where x and $(1-x)$ are the MgO and FeO mole fractions, respectively.

Equations 3 and 4 can be rearranged to express the mole fraction of each component in each phase as a function of pressure to obtain the curves shown in Fig. 4a:

$$x^{B1} = x^{B2} k_{MgO} \exp\{-\Delta V_{MgO} P/2RT\}$$

$$x^{B2} = \frac{1 - k_{FeO}\exp\{-\Delta V_{FeO}P/2RT\}}{k_{MgO}\exp\{-\Delta V_{MgO}P/2RT\} - k_{FeO}\exp\{-\Delta V_{FeO}P/2RT\}}$$

with

$$k_{MgO} = \exp\{\Delta V_{MgO} P^t_{MgO}/2RT\}$$

$$k_{FeO} = \exp\{\Delta V_{FeO} P^t_{FeO}/2RT\}$$

The volumes of MgO and FeO at the B1-B2 transition, as well as the transition pressures used to model the behavior of the $(Mg_x,Fe_{(1-x)})O$ binary system were obtained combining the results of this study and from literature (including our previous work on B1/B2 MgO)[13,14] and are reported in Supplementary Table 4. Note that we assumed temperature-independent values for the volumes and transition pressures at a fixed temperature of 4000 K.

In order to evaluate the density contrast within the mantle of a 5 $M_\oplus$ exoplanet, we used our linear mixing model to calculate the density of the Fe- and Mg- rich domains forming at 480 GPa (intermediate pressure in the coexisting region of a 60%-Mg initial composition) and 4000 K (Supplementary Fig. 14). Based on the phase loop shown in Fig. 4a of the main text, a representative initial B1-$(Mg_{0.6},Fe_{0.4})O$ solid solution would break down into B2-Fe-rich domains with composition B2-$(Mg_{0.4},Fe_{0.6})O$ and ρ=10.3 g/cm^3 and B1-MgO-rich ones with composition B1-$(Mg_{0.7},Fe_{0.3})O$ and ρ=8.7 g/cm^3, resulting in a 17% density contrast.

VI. IRON PARTITIONING AND MANTLE COMPOSITION

The partitioning of iron between post-perovskite (pPv) and ferropericlase (Fp) is given by the distribution coefficient, $K_D^{pPv/Fp}$, defined as:

$$K_D^{pPv/Fp} = \frac{X^{pPv}_{Fe}/X^{pPv}_{Mg}}{X^{Fp}_{Fe}/X^{Fp}_{Mg}}$$

where X is the mole fraction of Fe or Mg in the respective phase. In general, measuring $K_D^{pPv/Fp}$ under lower mantle conditions is very challenging and the reported experimental results are highly scattered. Within the stability field of post-perovskite, recent measurements generally report $\sim$ 0.1-0.2. That is, iron partitions strongly into ferropericlase over post-perovskite [72–74].

Measured partition coefficients can be sensitive to a number of factors including pressure, temperature, oxidation state, bulk iron content and other variables. As existing measurements and theoretical calculations extend only to $\sim$150 GPa, predicting the partition coefficients at conditions of the deep mantle of large rocky exoplanets is highly uncertain. Assuming the experimental values hold together with the expectation that rocky exoplanets will exhibit a wide range of (Mg+Fe)/Si and Mg# = Mg/(Mg+Fe) values in their interior, reflecting the wide compositional range in exoplanet host stars[2], it is likely that Fe-rich ferropericlase will be an important component of many rocky exoplanet interiors. As a specific example, the composition we have chosen here, $(Mg_{0.6},Fe_{0.4})O$, could arise from the following scenario: a mantle composed of 80% post-perovskite and 20% ferropericlase ((Mg+Fe)/Si = 1.25), bulk mantle Mg# =0.87 and a $K_D^{pPv/Fp}$ value of 0.1, yielding iron-depleted post-perovskite of composition $(Mg_{0.94},Fe_{0.06})SiO_3$ and iron-rich ferropericlase with composition $(Mg_{0.6},Fe_{0.4})O$ (Table 5). Experimental density data of pPv do not extend up to the pressures considered here, but according to X-ray diffraction measurements at $\sim$150 GPa and $\sim$2700 K[75] its density could be as low as 6 g/cm^3. Such a mantle would be characterized by large density gradients, especially at pressures exceeding the B1/B2 phase transition in FeO, where an additional density contrast arises between the dissociated B2-Fe-rich and B1-Mg-rich domains (Supplementary Fig. 14).

VII. SUPPLEMENTARY FIGURES AND TABLES

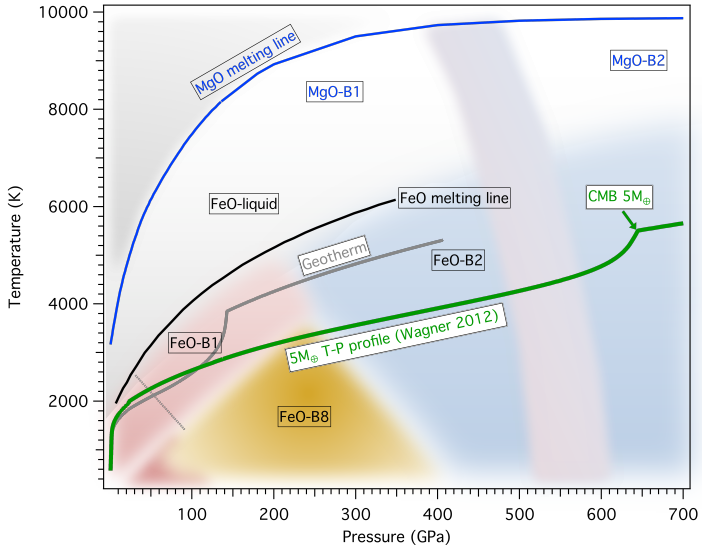

Supplementary Figure 1. The pressure-temperature profile of the Earth (grey geotherm) and of a 5 $M_\oplus$ exoplanet[6] (green curve) are shown together with the solid-solid phase boundaries and melting lines for MgO and FeO, the end-members of the ferropericlase solid solution. It can be observed that periclase and wüstite are expected to remain solid in the mantle of such bodies and go through phase transitions that do not happen within the Earth's mantle. Melting curves are extrapolated from Refs.[66,76], solid phase boundaries for FeO are from Refs.[13,25,26,30] and for MgO from Refs.[14,18].

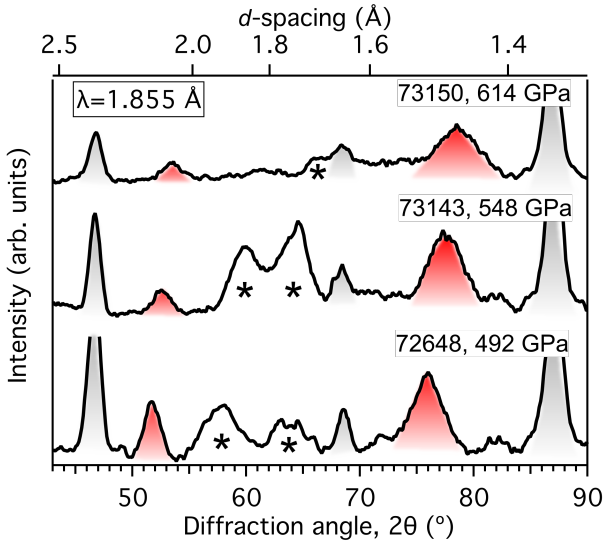

Supplementary Figure 2. One-dimensional integration of the diffraction data collected in this study using Fe X-ray source (λ=1.855Å). Peaks highlighted by red shaded area are from the (100) and (110) reflections of B2-FeO and grey peaks are from the Ta reference material. Asterisks point to the peaks due to single-crystal diamonds.

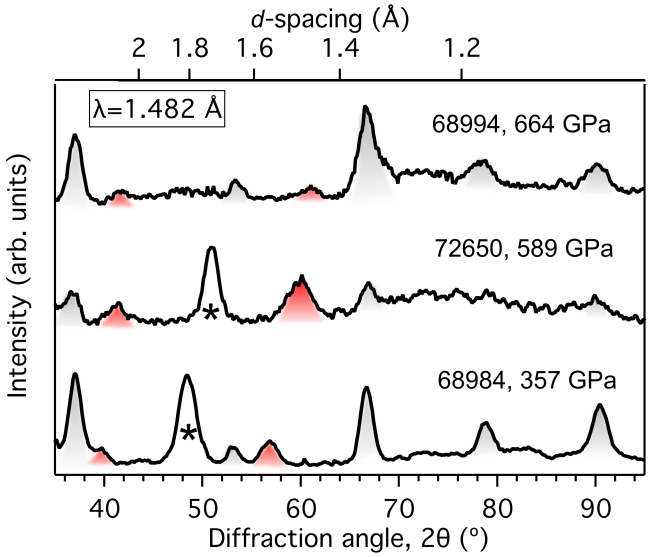

Supplementary Figure 3. One-dimensional integration of the diffraction data collected in this study using Cu X-ray source (λ=1.482Å). Peaks highlighted by red shaded area are from the (100) and (110) reflections of B2-FeO and grey peaks are from the Ta reference material. Asterisks point to the peaks due to single-crystal diamonds.

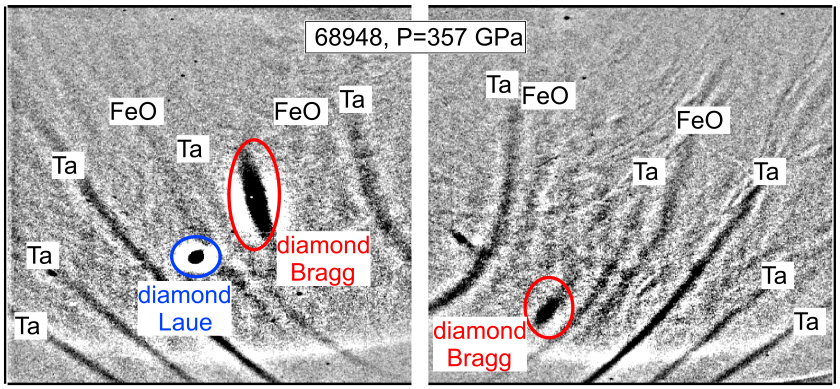

Supplementary Figure 4. Representative X-ray diffraction patterns for experiment 68948 showing two-dimensional data in the experimental geometry after background subtraction[55]. Red circles highlight Bragg diffraction peaks from ramp-compressed single-crystal diamond, while the blue circle points to a Laue diffraction spot due to the continuum component of the X-ray source spectrum[53]. Diffraction signals from FeO and Ta are continuous and characteristic of randomly-oriented polycrystalline materials.

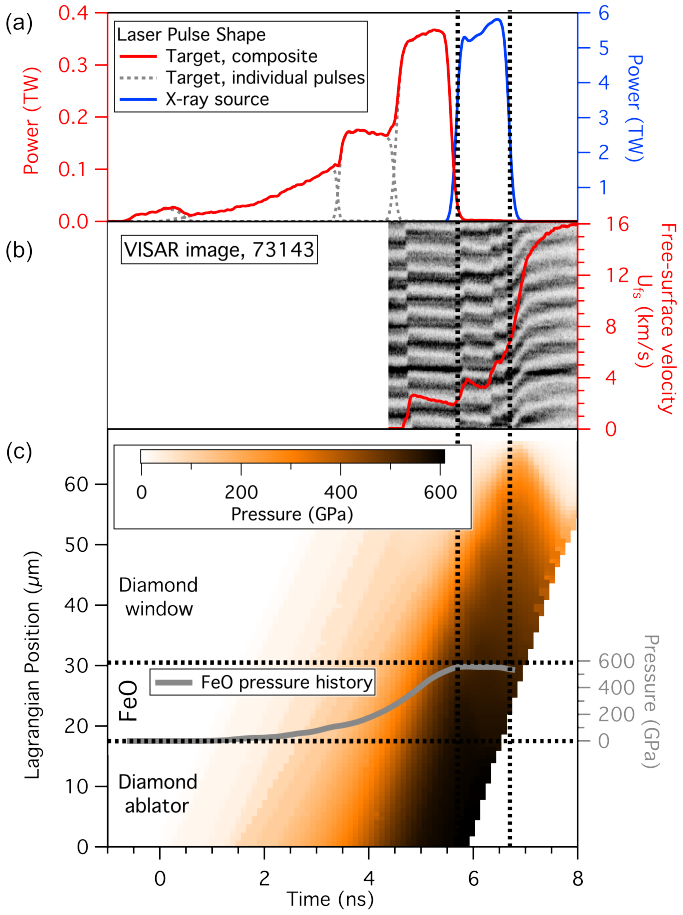

Supplementary Figure 5. (a) Representative composite pulse shape used to ramp-compress the target package (red curve, left axis) and corresponding pulse used to generate the X-ray source (blue curve, right axis). (b) VISAR data for experiment 73143 and corresponding free surface velocity (red, right axis). The first rise in U_{fs} at about 4.8 ns corresponds to the elastic wave of diamond emerging in the ablator and reaching the window free-surface after propagating through the target package. This generates a ∼50 GPa initial shock into the FeO. The compression proceeds through wave reverberations within the sample layer, that generates complex wave interactions reflected in the step-wise diamond free-surface velocity history. (c) Map of the pressure states within the target assembly as a function of Lagrangian position (vertical axis) and time (horizontal axis) as obtained by the backward-propagation of the measured free surface velocity of the diamond window. Horizontal dashed lines indicate the different layers of the target (17.5 μm diamond ablator, 13 μm FeO and 37 μm diamond window for this particular experiment). The vertical dashed lines indicate the time of the X-ray exposure (1-ns long). The central part of the map shows the average pressure history within the FeO layer (grey curve, right axis).

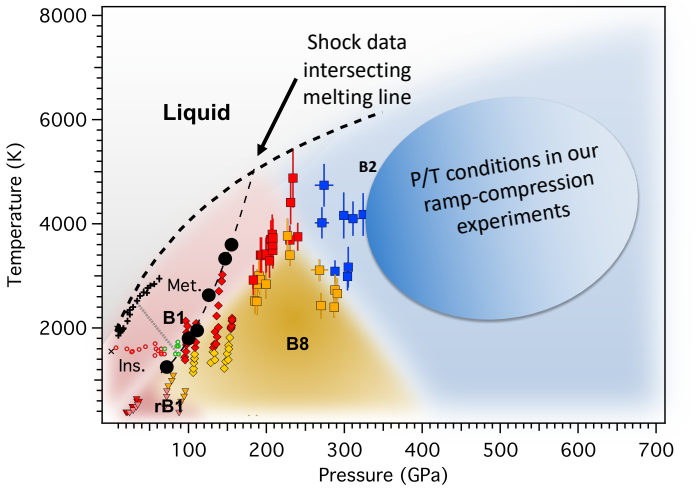

Supplementary Figure 6. Phase diagram of FeO. The color of the shaded area and symbols indicate the stability of the different structures: B1 in red, rhombohedral-B1 in pink, B8 in yellow and B2 in blue. The dark-blue circle corresponds to the estimated temperature in our ramp compression experiments. Empty circles are data from Ref.[27], reverse triangles from Ref.[26], squares from Ref.[13] and diamonds from Ref.[30]. The dashed grey line represents the insulator-to-metal transition observed within the B1 structure reported in Ref.[25]. Solid black circles are shock experiments from Ref.[67]. Black crosses indicate the melting curve measured in Ref.[77] and the dashed black line is the calculated melting line from Ref.[66].

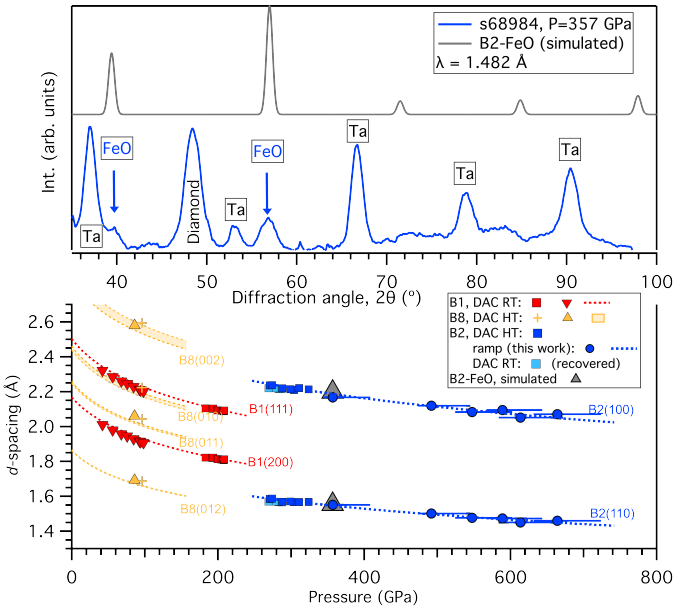

Supplementary Figure 7. Top: Diffraction data for experiment 68984 (blue) compared with the simulated diffraction pattern for B2-FeO (grey), using the volume determined experimentally in this work. Bottom: grey triangles indicate the expected *d*-spacings for the B2 structure at 357 GPa. The experimentally observed peaks match the two most intense reflections for B2-FeO.

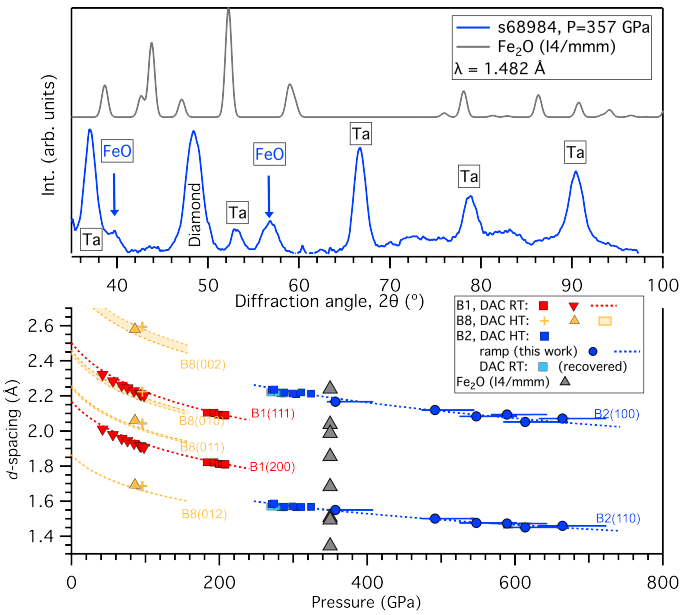

Supplementary Figure 8. Top: Diffraction data for experiment 68984 (blue) compared with the expected pattern for Fe_2O (grey). Bottom: grey triangles indicate the d-spacings for this new stoichiometry expected to be stable at 350 GPa. Experimentally we observe two peaks for FeO at 2θ ∼40° and 2θ ∼57° and they do not match the expected position of the most intense peak for Fe_2O.

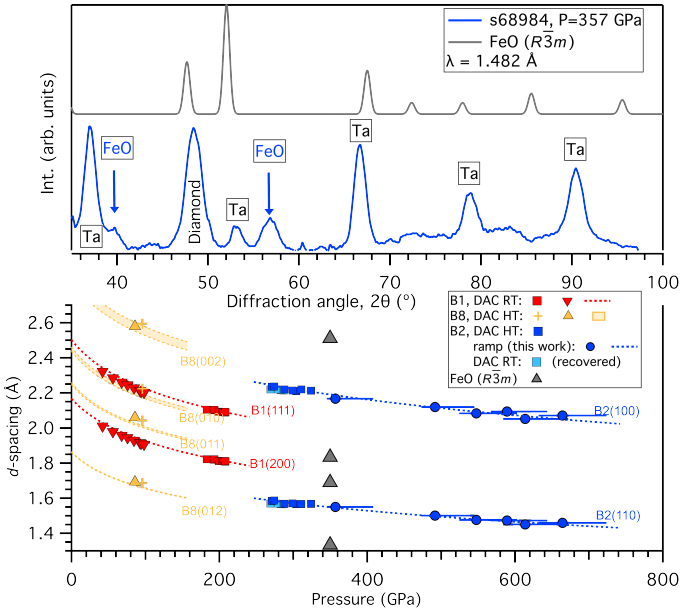

Supplementary Figure 9. Top: Diffraction data for experiment 68984 (blue) compared with the expected diffraction for stoichiometric FeO with space group $R\bar{3}m$ (grey). Bottom: grey triangles indicate the d-spacings for stoichiometric FeO ($R\bar{3}m$) predicted to be stable at 350 GPa. The proposed structure does not reproduce the experimentally observed peaks for FeO at 2θ ∼40° and 2θ ∼57°.

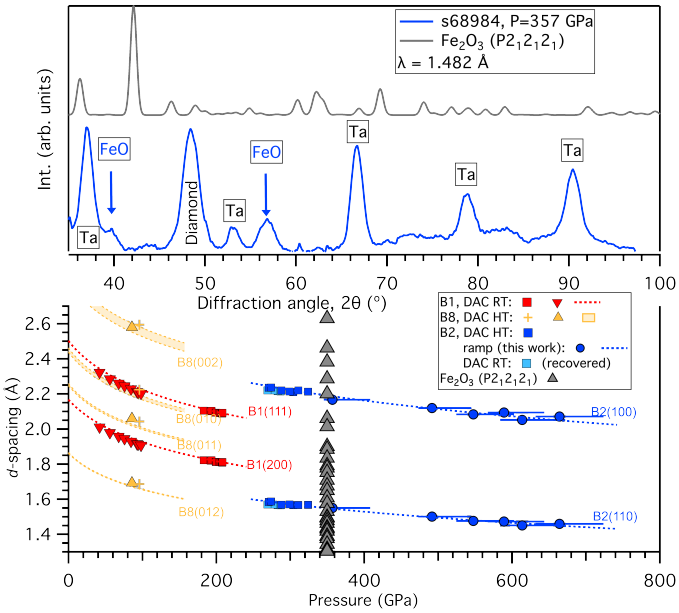

Supplementary Figure 10. Top: Diffraction data for experiment 68984 (blue) compared with the expected diffraction pattern for Fe_2O_3 (grey). Bottom: grey triangles indicate the d-spacings for this structure expected to be stable at 350 GPa. In addition to the main peak at 2θ ∼42° (which is close to the experimentally observed one), the diffraction signal for Fe_2O_3 with space group $P2_12_12_1$ is characterized by a series of lower intensity peaks in the range 2θ ∼46°-100°, that cannot explain the observation of an isolated intense peak at 2θ ∼57° in the experimental data.

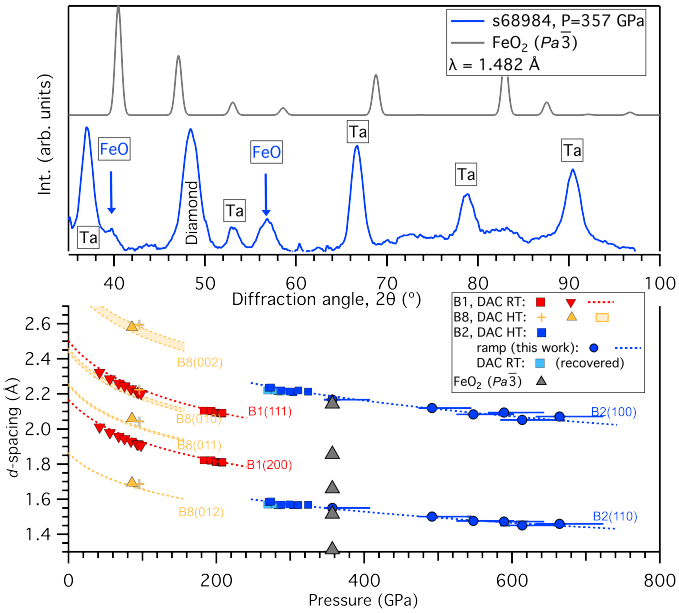

Supplementary Figure 11. Top: Diffraction data for experiment 68984 (blue) compared with the expected pattern for FeO_2 with space group $Pa\bar{3}$ (grey). Ref.[31] only reports the volume at 100 GPa, therefore we calculate the diffraction pattern using the volume obtained experimentally at 357 GPa, to facilitate the comparison with the experimental data. Bottom: grey triangles indicate the d-spacings for this structure at 357 GPa. Although the peak at 2θ ∼40° is very close to the observed one, we do not observe the second most intense peak at 2θ ∼48° (or d=1.84 Å) (the observed signal at 2θ ∼49° has the characteristic texture of the diamond reflections). Additionally, the most intense experimental peak for FeO is at 2θ ∼57° where the calculated structure only shows two low intensity reflections, whose Bragg angles do not match the experimental one.

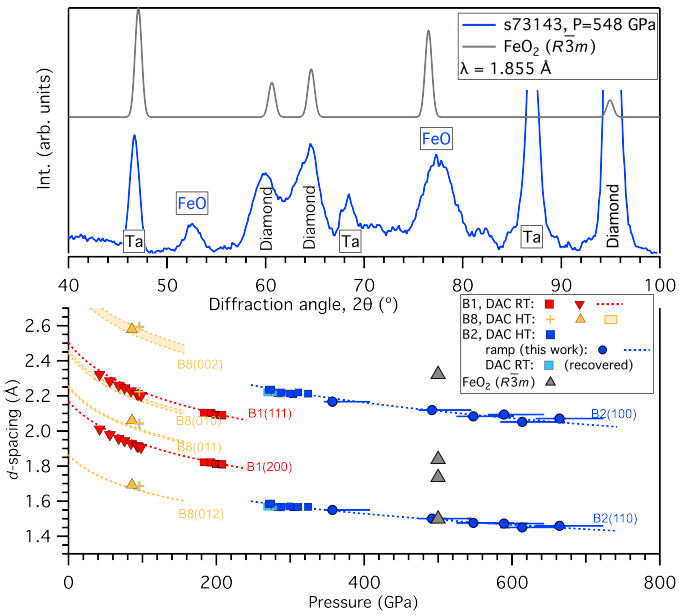

Supplementary Figure 12. Top: Diffraction data for experiment 73143 (blue) compared with the expected pattern for FeO_2 (grey). Bottom: grey triangles indicate the *d*-spacings for this structure expected to be stable at 500 GPa. Although one of the peaks for this structure is very close to the observed signal at 2θ ∼78°, this structure cannot reproduce the measured diffraction peak at 2θ ∼52°.

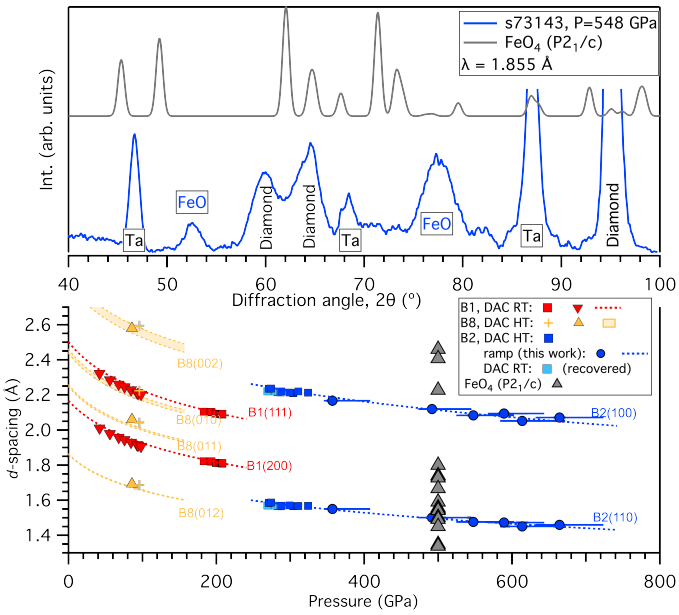

Supplementary Figure 13. Top: Diffraction data for experiment 73143 (blue) compared with the expected diffraction pattern for FeO_4 (grey). Bottom: grey triangles indicate the *d*-spacings for this structure expected to be stable at 500 GPa. Its diffraction pattern is characterized by many peaks that cannot explain the experimentally observed ones at 2θ ∼52° and 2θ ∼78°.

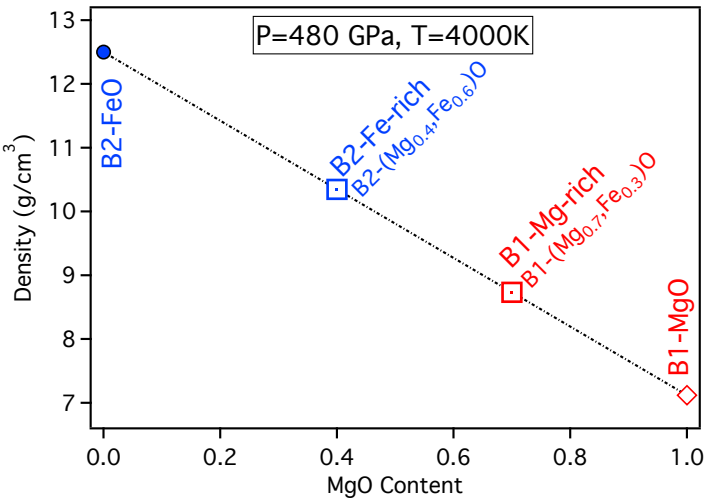

Supplementary Figure 14. Density variation of the B1/B2 mixed phase at 480 GPa and 4000 K as a function of MgO content. The densities of the end-members are from this study (experiment 72648 at 492 GPa) and Ref.[14] and they are linearly interpolated to estimate the densities of the B2-Fe-rich domains and of the B1-Mg-rich ones.

hkl	*d*-spacing (Å)
111	2.487
200	2.154
220	1.522

Supplementary Table 1. *d*-spacings of the intial Fe_xO powder corresponding to the (111), (200) and (220) reflections of the B1 phase as obtained from laboratory X-ray diffraction.

FeO	B1	B8	B2
ρ_0 (g/cm^3)	6.04±0.20	5.9±0.2	6.0±0.1
K_0 (GPa)	149.4±1.0	137.8±0.9	150 (fix)
$K_0^{'}$	4.1±0.3	4.1±3	4.4±0.2
MgO	B1		B2
ρ_0 (g/cm^3)	3.58		3.71±0.1
K_0 (GPa)	162.5		161±9
$K_0^{'}$	4.1±0.2		4.6±0.4

Supplementary Table 2. Equation of state parameters for FeO and MgO. Density, bulk modulus and pressure derivative for the three polymorphs of wüstite, as well as for the B1 and B2 MgO phases (from Ref.[14]). Parameters for the B1 and B8 FeO structures are from Ref.[30], B2 parameters are from this work.

Experiment	Pressure (GPa)	*d*(100) (Å)	*d*(110) (Å)	ρ (g/cm^3)
68984	357 (+51, -11)	2.17± 0.03	1.55± 0.01	11.4± 0.2
72648	492 (+53, -18)	2.119± 0.007	1.500± 0.007	12.5± 0.1
73143	548 (+55, -23)	2.08± 0.01	1.476± 0.006	13.1± 0.1
72650	589 (+55, -22)	2.09± 0.01	1.473± 0.004	13.2± 0.1
73150	614 (+58, -30)	2.051± 0.006	1.450± 0.005	13.83± 0.09
68994	664 (+60, -33)	2.07± 0.01	1.459± 0.005	13.5± 0.1

Supplementary Table 3. Summary of experimental results on the B2-FeO from our ramp-compression XRD measurements.

Parameter		Reference
P^t_{MgO}	600 GPa	Ref.[14]
P^t_{FeO}	270 GPa	Ref.[13] and this work
V^{B1}_{MgO}	5.5e-6 m^3/mol	Ref.[14]
V^{B2}_{MgO}	5.2e-6 m^3/mol	Ref.[14]
V^{B1}_{FeO}	6.6e-6 m^3/mol	Ref.[13]
V^{B2}_{FeO}	6.3e-6 m^3/mol	Ref.[13] and this work

Supplementary Table 4. Parameters used in the mixing model for the MgO-FeO binary system.

	$K_D^{pPv/Fp}$	Bulk Mg#	X_{pPv}	X_{Fp}	(Mg+Fe)/Si	pPv composition	Fp composition
case 1	0.1	0.87	0.8	0.2	1.25	$(Mg_{0.94},Fe_{0.06})SiO_3$	$(Mg_{0.6},Fe_{0.4})$
case 2	0.2	0.83	0.8	0.2	1.25	$(Mg_{0.87},Fe_{0.13})SiO_3$	$(Mg_{0.6},Fe_{0.4})$

Supplementary Table 5. Two representative scenarios yielding an $(Mg_{0.6}Fe_{0.4})O$ ferropericlase composition in an exoplanet mantle. $K_D^{pPv/Fp}$ = distribution coefficient, Bulk Mg# = Mg/(Mg+Fe) for bulk composition, X_{pPv} and X_{Fp} = mole fraction of post-perovskite and ferropericlase, respectively.

VIII. REFERENCES

[1]Unterborn, C. T. & Panero, W. R. The pressure and temperature limits of likely rocky exoplanets. *Journal of Geophysical Research: Planets* **124**, 1704–1716 (2019).

[2]Hinkel, N. R. & Unterborn, C. T. The star-planet connection. I. Using stellar composition to observationally constrain planetary mineralogy for the 10 closest stars. *The Astrophysical Journal* **853**, 83 (2018). 1709.08630.

[3]Valencia, D., O'Connell, R. J. & Sasselov, D. Internal structure of massive terrestrial planets. *Icarus* **181**, 545–554 (2006).

[4]Seager, S., Kuchner, M., Hier-Majumder, C. A. & Militzer, B. Mass-radius relationships for solid exoplanets. *The Astrophysical Journal* **669**, 1279–1297 (2007).

[5]Unterborn, C. T., Dismukes, E. E. & Panero, W. R. Scaling the Earth: a sensitivity analysis of terrestrial exoplanetary interior models. *The Astrophysical Journal* **819**, 32 (2016).

[6]Wagner, F. W., Tosi, N., Sohl, F., Rauer, H. & Spohn, T. Rocky super-Earth interiors. Structure and internal dynamics of CoRoT-7b and Kepler-10b. *Astronomy & Astrophysics* **541**, A103 (2012).

[7]Boujibar, A., Driscoll, P. & Fei, Y. Super-Earth internal structures and initial thermal states. *Journal of Geophysical Research: Planets* **125** (2020).

[8]Duffy, T., Madhusudhan, N. & Lee, K. K. *Mineralogy of Super-Earth Planets*, vol. 2 (Elsevier B.V., Oxford, 2015).

[9]Umemoto, K. *et al.* Phase transitions in $MgSiO_3$ post-perovskite in super-Earth mantles. *Earth and Planetary Science Letters* **478**, 40–45 (2017).

[10]Bitsch, B. & Battistini, C. Influence of sub- and super-solar metallicities on the composition of solid planetary building blocks. *Astronomy & Astrophysics* **633**, A10 (2020).

[11]Scora, J., Valencia, D., Morbidelli, A. & Jacobson, S. Chemical diversity of super-Earths as a consequence of formation. *Monthly Notices of the Royal Astronomical Society* **493**, 4910–4924 (2020).

[12]Jang, B. G., Kim, D. Y. & Shim, J. H. Metal-insulator transition and the role of electron correlation in FeO_2. *Physical Review B* **95**, 1–5 (2017).

[13]Ozawa, H., Takahashi, F., Hirose, K., Ohishi, Y. & Hirao, N. Phase transition of FeO and stratification in Earth's outer core. *Science* **334**, 792–794 (2011).

[14]Coppari, F. *et al.* Experimental evidence for a phase transition in magnesium oxide at exoplanet pressures. *Nature Geoscience* **6**, 926–929 (2013).

[15]Duffy, T. S., Hemley, R. J. & Mao, H.-k. Equation of state and shear strength at multimegabar pressures: magnesium oxide to 227 GPa. *Physical Review Letters* **74**, 1371–1374 (1995).

[16]Dorfman, S. M., Prakapenka, V. B., Meng, Y. & Duffy, T. S. Intercomparison of pressure standards (Au, Pt, Mo, MgO, NaCl and Ne) to 2.5 Mbar. *Journal of Geophysical Research* **117**, B08210 (2012).

[17]McWilliams, R. S. *et al.* Phase transformations and metallization of magnesium oxide at high pressure and temperature. *Science* **338**, 1330–1333 (2012).

[18]Bouchet, J. *et al. Ab initio* calculations of the B1-B2 phase transition in MgO. *Physical Review B* **99**, 1–10 (2019).

[19]Musella, R., Mazevet, S. & Guyot, F. Physical properties of MgO at deep planetary conditions. *Physical Review B* **99**, 1–8 (2019).

[20]Soubiran, F. & Militzer, B. Anharmonicity and phase diagram of magnesium oxide in the megabar regime. *Physical Review Letters* **125**, 175701 (2020).

[21]Lazicki, A. *et al.* Metastability of Diamond Ramp-Compressed to 2 TPa. *To be published on Nature* (2020).

[22]Mao, H.-k., Shu, J., Fei, Y., Hu, J. & Hemley, R. J. The wüstite enigma. *Physics of the Earth and Planetary Interiors* **96**, 135–145 (1996).

[23]Fei, Y. Crystal chemistry of FeO at high pressure and temperature. *Mineral Spectroscopy: A tribute to Roger G. Burns* **5**, 243–254 (1996).

[24]Sata, N. *et al.* Compression of FeSi, Fe_3C, $Fe_{0.95}O$, and FeS under the core pressures and implication for light element in the Earth's core. *Journal of Geophysical Research* **115**, B09204 (2010).

[25]Ohta, K. *et al.* Experimental and theoretical evidence for pressure-induced metallization in FeO with rocksalt-type structure. *Physical Review Letters* **108**, 026403 (2012).

[26]Fei, Y. & Mao, H. K. In situ determination of the NiAs phase of FeO at high pressure and temperature. *Science (New York, N.Y.)* **266**, 1678–1680 (1994).

[27]Murakami, M. *et al.* High pressure and high temperature phase transitions of FeO. *Physics of the Earth and Planetary Interiors* **146**, 273–282 (2004).

[28]Campbell, A. J. *et al.* High pressure effects on the iron-iron oxide and nickel-nickel oxide oxygen fugacity buffers. *Earth and Planetary Science Letters* **286**, 556–564 (2009).

[29]Ozawa, H., Hirose, K., Tateno, S., Sata, N. & Ohishi, Y. Phase transition boundary between B1 and B8 structures of FeO up to 210 GPa. *Physics of the Earth and Planetary Interiors* **179**, 157–163 (2010).

[30]Fischer, R. A. *et al.* Equation of state and phase diagram of FeO. *Earth and Planetary Science Letters* **304**, 496–502 (2011).

[31]Weerasinghe, G. L., Pickard, C. J. & Needs, R. J. Computational searches for iron oxides at high pressures. *J. Phys.: Condens. Matter* **27**, 455501 (2015).

[32]Lavina, B. *et al.* Discovery of the recoverable high-pressure iron oxide Fe_4O_5. *Proceedings of the National Academy of Sciences of the United States of America* **108**, 17281–17285 (2011).

[33]Hu, Q. *et al.* FeO_2 and FeOOH under deep lower-mantle conditions and Earth's oxygen-hydrogen cycles. *Nature* **534**, 241–244 (2016).

[34]Vassiliou, M. S. & Ahrens, T. J. The equation of state of $Mg_{0.6}Fe_{0.4}0$ to 200 GPa. *Geophysical Research Letters* **9**, 127–130 (1982).

[35]Zhang, N. B. *et al.* Spin transition of ferropericlase under shock compression. *AIP Advances* **8**, 075028 (2018).

[36]Deng, J. & Lee, K. K. Viscosity jump in the lower mantle inferred from melting curves of ferropericlase. *Nature Communications* **8** (2017).

[37]Kondo, T., Ohtani, E., Hirao, N., Yagi, T. & Kikegawa, T. Phase transitions of (Mg,Fe)O at megabar pressures. *Physics of the Earth and Planetary Interiors* **143-144**, 201–213 (2004).

[38]Wicks, J. K. *et al.* Thermal equation of state and stability of $(Mg_{0.06}Fe_{0.94})O$. *Physics of the Earth and Planetary Interiors* **249**, 28–42 (2015).

[39]McCammon, C. A., Ringwood, A. E. & Jackson, I. Thermodynamic of the system Fe-FeO-MgO at high pressure and temperature and a model for formation fo the Earth's core. *Geophys. J. R. Astr. Soc.* **72**, 577 (1983).

[40]Dubrovinsky, L. S. *et al.* Stability of Ferropericlase in the Lower Mantle. *Science* **289**, 430–433 (2000).

[41]Murakami, M., Hirose, K., Kawamura, K., Sata, N. & Ohishi, Y. Post-Perovskite Phase Transition in $MgSiO_3$. *Science* **304**, 855 (2004).

[42]Ritterbex, S., Harada, T. & Tsuchiya, T. Vacancies in MgO at ultrahigh pressure: About mantle rheology of super-Earths. *Icarus* **305**, 350–357 (2018).
[43]Karato, S.-i. Rheological structure of the mantle of a super-Earth: Some insights from mineral physics. *Icarus* **212**, 14–23 (2011).
[44]Reali, R. *et al.* Modeling viscosity of (Mg,Fe)O at lowermost mantle conditions. *Physics of the Earth and Planetary Interiors* **287**, 65–75 (2019).
[45]Thielmann, M., Golabek, G. J. & Marquardt, H. Ferropericlase control of lower mantle rheology: impact of phase morphology. *Geochemistry, Geophysics, Geosystems* **21** (2020).
[46]Shahnas, M. H., Pysklywec, R. N. & Yuen, D. A. Penetrative convection in super-Earth planets: consequences of $MgSiO_3$ postperovskite dissociation transition and implications for super-Earth GJ 876 d. *Journal of Geophysical Research: Planets* **123**, 2162–2177 (2018).
[47]Yamazaki, D., Yoshino, T., Matsuzaki, T., Katsura, T. & Yoneda, A. Texture of (Mg,Fe)SiO_3 perovskite and ferro-periclase aggregate: Implications for rheology of the lower mantle. *Physics of the Earth and Planetary Interiors* **174**, 138–144 (2009).
[48]Stamenković, V., Breuer, D. & Spohn, T. Thermal and transport properties of mantle rock at high pressure: Applications to super-Earths. *Icarus* **216**, 572–596 (2011).
[49]Tackley, P. J., Ammann, M., Brodholt, J. P., Dobson, D. P. & Valencia, D. Mantle dynamics in super-Earths: Post-perovskite rheology and self-regulation of viscosity. *Icarus* **225**, 50–61 (2013).
[50]Vilim, R., Stanley, S. & Elkins-Tanton, L. The effect of lower mantle metallization on magnetic field generation in rocky exoplanets. *Astrophysical Journal Letters* **768** (2013).
[51]McCammon, C. A. & Liu, L.-g. The effects of pressure and temperature on nonstoichiometric Wüstite, Fe_xO: the iron-rich phase boundary. *Phys Chem Minerals* **10**, 106–113 (1984).
[52]Boehly, T. R. *et al.* Initial performance results of the OMEGA laser system. *Optics Communication* **133**, 495–506 (1997).
[53]Coppari, F. *et al.* Optimized x-ray sources for x-ray diffraction measurements at the Omega Laser Facility. *Review of Scientific Instruments* **90**, 125113 (2019).
[54]Celliers, P. M. *et al.* Line-imaging velocimeter for shock diagnostics at the OMEGA laser facility. *Review of Scientific Instruments* **75**, 4916–4929 (2004).
[55]Rygg, J. R. *et al.* Powder diffraction from solids in the terapascal regime. *Review of Scientific Instruments* **83**, 113904 (2012).
[56]Rygg, J. R. *et al.* X-ray diffraction at the National Ignition Facility. *Review of Scientific Instruments* **91** (2020).
[57]Maw, J. R. A characteristics code for analysis of isentropic compression experiments. *AIP Conference Procedings* **706**, 1217–1220 (2004).
[58]Rothman, S. D. & Maw, J. Characteristics analysis of isentropic compression experiments (ICE). *J. Phys. IV France* **134**, 745–750 (2006).
[59]Bradley, D. K. *et al.* Diamond at 800 GPa. *Physical Review Letters* **102**, 75503 (2009).
[60]Wicks, J. K. *et al.* Crystal structure and equation of state of Fe-Si alloys at super-Earth core conditions. *Scientific Advances* **4**, eaao5864 (2018).
[61]Lazicki, A. *et al.* X-ray diffraction of solid tin up to 1.2 TPa. *Physical Review Letters* **115**, 075502 (2015).
[62]Wang, J. *et al.* X-ray diffraction of molybdenum under ramp compression to 1 TPa. *Physical Review B* **94**, 104102 (2016).
[63]Polsin, D. N. *et al.* Measurement of Body-Centered-Cubic Aluminum at 475 GPa. *Physical Review Letters* **119**, 175702 (2017).
[64]Millot, M. *et al.* Nanosecond X-ray diffraction of shock-compressed superionic water ice. *Nature* **569**, 251–255 (2019).
[65]Kraus, R. G. *et al.* Dynamic compression of copper to over 450 GPa: A high-pressure standard. *Physical Review B* **93**, 134105 (2016).
[66]Komabayashi, T. Thermodynamics of melting relations in the system Fe-FeO at high pressure: Implications for oxygen in the Earth's core. *Journal of Geophysical Research: Solid Earth* **119**, 1–14 (2014).
[67]Knittle, E., Jeanloz, R., Mitchell, A. C. & Nellis, W. J. Metallization of $Fe_{0.94}O$ at elevated pressures and temperatures observed by shock-wave electrical resistivity measrurements. *Solid State Communication* **59**, 513–515 (1986).
[68]Fei, Y. & Saxena, S. K. A thermochemical data base for phase equilibria in the system Fe-Mg-Si-O at high pressure and temperature. *Phys Chem Minerals* **13**, 311 (1986).
[69]Ovsyannikov, S. V., Shchennikov, V. V., Shvetsova, M. A., Dubrovinsky, L. S. & Polian, A. Tuning of the stoichiometry of $Fe_{1-x}O$ wüstite by compression. *Physical Review B* **81**, 060101 (2010).
[70]Liu, L. G., Bassett, W. A. & Liu, M. S. Polymorphism in the solid solutions, potassium chloride-sodium chloride and rubidium chloride-potassium chloride, at high pressure. *Journal of Physical Chemistry* **77**, 1695–1699 (1973).
[71]Stixrude, L. Structure and sharpness of phase transitions and mantle discontinuities. *Journal of Chemical Physics* **102**, 14835 (1997).
[72]Sinmyo, R., Hirose, K., Muto, S., Ohishi, Y. & Yasuhara, A. The valence state and partitioning of iron in the Earth's lowermost mantle. *Journal of Geophysical Research: Solid Earth* **116**, 1–9 (2011).
[73]Piet, H. *et al.* Spin and valence dependence of iron partitioning in Earth's deep mantle. *Proceedings of the National Academy of Sciences of the United States of America* **113**, 11127–11130 (2016).
[74]Gialampouki, M. A., Xu, S. & Morgan, D. Iron valence and partitioning between post-perovskite and ferropericlase in the Earth's lowermost mantle. *Physics of the Earth and Planetary Interiors* **282**, 110–116 (2018).
[75]Sakai, T., Dekura, H. & Hirao, N. Experimental and theoretical thermal equations of state of $MgSiO_3$ post-perovskite at multi-megabar pressures. *Scientific Reports* **6**, 6–13 (2016).
[76]Alfè, D. Melting curve of MgO from first-principles simulations. *Physical Review Letters* **94**, 235701 (2005).
[77]Fischer, R. A. & Campbell, A. J. High-pressure melting of wüstite. *American Mineralogist* **95**, 1473–1477 (2010).